

Modeling Scattering Coefficients using Self-Attentive Complex Polynomials with Image-based Representation

Andrew Cohen^{* 1} Weiping Dou¹ Jiang Zhu¹ Slawomir Koziel² Peter Renner¹ Jan-Ove Mattsson¹
Xiaomeng Yang¹ Beidi Chen¹ Kevin Stone¹ Yuandong Tian^{* 1}

Abstract

Finding antenna designs that satisfy frequency requirements and are also optimal with respect to multiple physical criteria is a critical component in designing next generation hardware. However, such a process is non-trivial because the objective function is typically highly nonlinear and sensitive to subtle design change. Moreover, the objective to be optimized often involves electromagnetic (EM) simulations, which is slow and expensive with commercial simulation software. In this work, we propose a sample-efficient and accurate surrogate model, named **CZP** (Constant Zeros Poles), to directly estimate the *scattering coefficients* in the frequency domain of a given 2D planar antenna design, without using a simulator. **CZP** achieves this by predicting the complex zeros and poles for the frequency response of scattering coefficients, which we have theoretically justified for any linear PDE, including Maxwell's equations. Moreover, instead of using low-dimensional representations, **CZP** leverages a novel image-based representation for antenna topology inspired by the existing mesh-based EM simulation techniques, and attention-based neural network architectures. We demonstrate experimentally that **CZP** not only outperforms baselines in terms of test loss, but also is able to find 2D antenna designs verifiable by commercial software with only 40k training samples, when coupling with advanced sequential search techniques like reinforcement learning.

1. Introduction

The next generation of Metaverse computing devices such as virtual reality (VR) and augmented reality (AR) offers

^{*}Equal contribution ¹Meta AI ²Reykjavic University. Correspondence to: Andrew Cohen <andrewcohen@meta.com>, Yuandong Tian <yuandong@meta.com>.

exciting possibilities for immersion in the digital world. In pursuit of seamless wireless connectivity with high wireless throughput and low latency to enable such user experiences, antenna design has become even more challenging than ever before. This is because the antenna's physical volume has been constrained by the stylish, light-weight industrial design requirements for wearable devices, while the demand for broader spectrum coverage to support the AR/VR experiences has been ever growing. To meet the demand, one device contains up to 10 to 20 antennas in a small form factor. Moreover, the recent adoption of WiFi 6E in the consumer electronic products such as Meta's Quest 2, extends the WiFi high band to the entire 6GHz spectrum, which presents a significant new challenge in antenna design. From the wireless industry perspective, there is a demand to design and optimize antennas that can unleash their full potential under the given space constraints.

Computational antenna design heavily relies on full-wave electromagnetic (EM) simulations. The process is expensive in terms of both simulation and engineer time as antenna engineers often iterate on antenna configurations using CPU-intensive commercial software (CST, 2021; XFD). This high computational overhead is the primary bottleneck in an antenna engineer's ability to rapidly experiment with different antenna geometric structures. A single simulation can take dozens of seconds to several weeks depending on the systematic complexity of a device. And this learning process is sequential because insights gained from simulating one set of candidate topologies are then used for generating the next set of candidates.

Commercial antenna software often uses mesh-based EM simulation. It involves finding a suitable mesh data structure to convert the underlying Maxwell partial differential equations (PDEs) of a system into ordinary differential equations (ODEs) that can be solved by finite difference methods (FDMs) (Yee, 1966). The mesh is often non-uniform, and typically with much higher resolution in regions of importance such as the boundaries of and borders between materials. It is not uncommon for a mesh to contain tens of millions of cells, leading to expensive and slow computation.

Developing cheaper alternatives to simulation is the focus of extensive research. Many works attempt to replace costly EM simulation with a lighter weight *surrogate model*, which trades off some degree of accuracy for computational efficiency. The surrogate model is then used by a downstream optimization procedure. In the EM based microwave circuit design, such as microwave filters, impedance-matching networks, multiplexers, etc., the equivalent-circuit, empirical, and semi-analytical models and combinations have been used as surrogate models with the links to the full-wave simulation (Rayas-Sanchez, 2004; Bakr et al., 2000). The same approaches have been rarely applied to antenna modeling, due to the fact that the radiating structures are too complex to lend themselves to analytical and/or circuit modeling. Broadly, there are two approaches to antenna surrogate modeling, coarser approximate physics-driven simulation (Zhu et al., 2007; Koziel & Ogurtsov, 2013) or data-driven methods which model the computation performed by the simulator (Koziel, 2017). In this work, we focus on the latter and leverage recent advances in machine learning to efficiently learn a surrogate model. It has been noted that machine learning has great promise which has not yet been fully realized in antenna design (Dou et al., 2022).

There are many challenges to learning a useful surrogate model. Theoretically, the antenna search space is high dimensional and the relationship between antenna topology and resonance profile is highly non-linear. However, state-of-the-art neural network architectures have demonstrated the ability to learn complicated relationships in many domains such as language (Brown et al., 2020), images (Ramesh et al., 2021) and molecules and proteins (Chilingaryan et al., 2022). Additionally, in the antenna space the cost of data is significant since it is typically collected from the commercial EM software which is computationally expensive.

In this work, we propose a novel surrogate model network architecture which addresses both difficulties raised above. It leverages a transformer-based encoder (Vaswani et al., 2017) to deal with the highly non-linear relationship of antenna topology and resonances and also incorporates domain-specific inductive biases to alleviate the issues posed by limited data. Here, we focus on the scattering coefficients of antennas, specifically the reflection coefficient which is used to describe an antenna’s resonant frequencies and operating bandwidth. The contributions of this work are 4-fold:

- Inspired by state-of-the-art mesh-based simulation techniques, we propose a novel image-based representation of antennas geometries that is both sample-efficient and captures the critical boundary information that is captured by high resolution meshes.
- We show that the resonance characteristic of an antenna can be written analytically as the ratio of two complex-

valued polynomials with a compact representation in terms of a constant, zeros and poles. Furthermore, this property holds for any linear PDE, beyond Maxwell’s equations.

- We propose a transformer architecture that first tokenizes the image representation and then directly predicts the complex valued zeros and poles of the S scattering matrix to compute the frequency response which we refer to as **CZP**.
- Experiments demonstrate the superiority of the **CZP** model over multiple baselines on test set loss. Furthermore, when coupled with an optimization procedure like reinforcement learning, **CZP** can find antenna topologies that are verified by commercial EM modeling software to meet design specifications. This shows that **CZP** not only generalizes to unseen designs, but also is robust to potentially adversarial designs found by the optimization procedure.

2. Antenna Preliminaries

In this section, we define key notions and concepts and also introduce the antenna design problem. Then, we present a derivation based on how traditional EM solvers compute the solution to Maxwell’s equations and is the theoretical innovation on which we base our **CZP** (Constant Zeros Poles) architecture.

2.1. Antenna Parameterization

In this work, we consider 2D planar antennas to demonstrate the approach. An antenna design consists of the following components:

Substrate. The rectangular printed circuitry board of width S_x and height S_y on which the other components sit. The substrate has thickness S_z and dielectric permittivity ϵ_r .

Ground plane. A solid rectangle extending through the entire substrate in the x direction and partially in the y direction.

Discrete port. The port location is the coordinate p_x, p_y and is dependent on one of the front-side metallic patches.

Front-side metallic patches. The antenna contains M rectangular metallic patches which can freely move within the substrate area or pre-determined ranges. The m -th patch p_m is defined by its width and height $s_{m,x}, s_{m,y}$ and, the coordinate of the bottom left corner $l_{m,x}, l_{m,y}$. When the boundary of a metallic patch goes beyond the substrate, the excess is simply clipped. When patches overlap, there is no increase in the thickness; they combine to make a single metallic patch that is no longer rectangular.

Combining all these specifications, we now have an overall

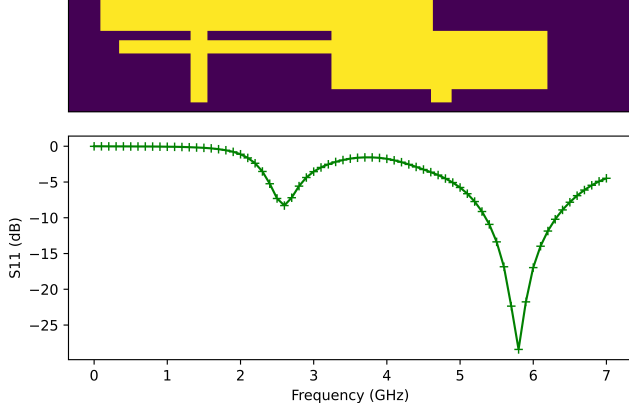


Figure 1. **Top:** An instance of an antenna from the five patch example in a AR device. Yellow corresponds to patches of metallic substrate and purple corresponds to the board on which the antenna sits. **Bottom:** The corresponding frequency response of the given antenna.

design choice vector defined as

$$\mathbf{h} = \{S_x, S_y, S_z, p_x, p_y, \{s_{m,x}, s_{m,y}, l_{m,x}, l_{m,y}\}_{m=1}^M\}, \quad (1)$$

which determines the antenna's *frequency response* described by the logarithm of modulus of the *scattering coefficients* $\log |S_{11}(\omega)|$, typically expressed in decibels (dB). $S_{11}(\omega)$, as a function of frequency ω , is defined as the following (Caspers, 2012):

$$S_{11}(\omega) := \frac{Z_{\text{in}}(\omega)/Z_0 - 1}{Z_{\text{in}}(\omega)/Z_0 + 1} \quad (2)$$

where $Z_{\text{in}}(\omega)$ is the input impedance of the antenna, determined by the design vector \mathbf{h} . Figure 1 shows an example antenna design and its $S_{11}(\omega)$.

The objective. Antenna engineers aim to find the right design choice \mathbf{h} so that specific antenna design targets are met over the frequency bands of interest, for example, there needs to be dips (i.e., more absorption) in $S_{11}(\omega)$ at WiFi 2.4GHz band and WiFi 5-7GHz band for WiFi 6E, as shown in Figure 1 bottom row.

Five Patch Example. In this work, we consider an antenna example with an FR-4 substrate that is 30mm by 6mm and 5 front-side metallic patches with fixed dimensions and location boundaries (see Appendix for details). Additionally, we assume that the only degrees of freedom are the locations $\{s_{m,x}, s_{m,y}\}$ of each of the 5 patches as defined by the coordinates of the bottom left corner. We constrain the problem as such for experimental simplicity and acknowledge this is a simplified setting with respect to production-tier antenna optimization. However, the proposed surrogate model is agnostic to the assumption on patches and the optimisation

procedure can be easily extended to variable patches of varying dimensions.

3. An analytical formula of scattering coefficients $S_{11}(\omega)$

The relationship between an antenna's topology and its responses is governed by the well-known Maxwell's equations which can be written in the form of PDEs. When solving Maxwell's equations, traditional methods discretize the space and convert the PDEs into the following ODEs (Weiland, 1977):

$$\dot{\phi} = A(\mathbf{h})\phi \quad (3)$$

where the vector ϕ contain electromagnetic quantities (e.g., electric/magnetic field strength and potentials, voltages and currents, etc) at each grid cell. Note that ϕ is indexed by spatial location \mathbf{x} : $\phi = [\phi(\mathbf{x}_1), \phi(\mathbf{x}_2), \dots]$ and thus is an infinite-dimensional vector in the continuous case and a vector of dimension N in finite difference methods. Finally, $A(\mathbf{h})$ is a matrix of size N -by- N related to material properties \mathbf{h} determined by the design, and topological structure of the discretized grid cells.

For better understanding, here we put a concrete example of Eqn. 3. Consider a one-dimensional wave equation $\frac{\partial^2 \psi}{\partial t^2} = c^2 \frac{\partial^2 \psi}{\partial x^2}$. Then by setting $\phi = [\psi(x_1), \dots, \psi(x_N), \frac{\partial \psi}{\partial t}(x_1), \dots, \frac{\partial \psi}{\partial t}(x_N)]^\top \in \mathbb{R}^{2N}$, the wave equation can be written in the form of Eqn. 3 with

$$A = \begin{bmatrix} 0 & 1 \\ c^2 B & 0 \end{bmatrix},$$

where $B \in \mathbb{R}^{N \times N}$ spatially discretizes the operator $\frac{\partial^2}{\partial x^2}$.

From the initial condition $\phi(\mathbf{x}, 0)$, classic techniques (e.g., finite element methods (Weiland, 1977)) simply perform temporal integration to get the spatial-temporal signal $\phi(\mathbf{x}, t)$, and compute $S_{11}(\omega)$ by its definition, which is time-consuming.

Instead, we choose to follow another path, by directly performing a temporal Fourier transform for ODEs. Following this, we show that $S_{11}(\omega)$ has an analytic form as the quotient of two complex polynomials with respect to frequency ω of the same order. This is presented formally in the following theorem:

Theorem 3.1 (Analytical Structure of Scattering Coefficients). *For ODE in the form of Eqn. 3, if $A(\mathbf{h})$ is diagonalizable, then the logarithm of modulus of the scattering coefficients $\log |S_{11}(\omega)|$ can be written as:*

$$\log |S_{11}(\omega)| = \log |c_0(\mathbf{h})| + \sum_{k=1}^K \log \frac{|\omega - z_k(\mathbf{h})|}{|\omega - p_k(\mathbf{h})|} \quad (4)$$

where the constant $c_0(\mathbf{h})$, zeros $\{z_k(\mathbf{h})\}_{k=1}^K$ and poles

$\{p_k(\mathbf{h})\}_{k=1}^K$ are complex numbers and all depend on $A(\mathbf{h})$ and thus functions of the design choice \mathbf{h} .

This motivates us to train a neural network to predict the zeros z_k (i.e., roots of the nominator) and poles p_k (i.e., roots of the denominator), as well as a global constant c_0 from material properties \mathbf{h} , in order to predict scatter coefficients S_{11} that are provided by existing commercial software as a supervision.

With this formulation, we avoid any forward numerical integration and arrive at the quantity we want in one inference pass. Again, we point out that our approach is general and not restricted to antenna design; For any linear PDE system that can be discretized into the form of Eqn. 3 where $A(\mathbf{h})$ does not vary with ϕ , its frequency response can be computed similarly.

4. Network Architecture

In this section, we discuss the details of the proposed model. Specifically, we propose a novel image representation for a 2D antenna inspired by the mesh representations commonly used by EM simulators. Then, following the analysis in the previous section, we introduce our image-based transformer architecture which predicts the zeros and poles of scattering coefficients.

4.1. Image representation

Mesh-based finite element methods underpin many of the available simulation tools in electromagnetics and other fields (Pardo et al., 2007). The mesh converts the underlying PDEs of the system into an ODE solvable by finite element methods (Weiland, 1977). Mesh representations use the fact that an antenna’s resonance characteristics are directly related to its local and global topological structure. This motivates the use of images for learning a surrogate model as it contains the same local and global spatial information. A model would have to cope with a naive representation (i.e. the coordinates of front-side metallic patches) by learning these spatial relationships.

A critical component of successful meshing is to generate non-uniform, adaptive meshes which allocate high resolution, dense meshing to areas in which the quantity ϕ may change rapidly (e.g., at sharp corners). Adaptive meshing enables the simulation of systems unsolvable by traditional discretization methods (Pfaff et al., 2021). Guided by this, we posit that an image representation of an antenna should provide the key regions (i.e., boundaries and corners of substrate) explicitly so that a neural network does not need to spend unnecessary computation learning these features.

We propose a three channel image representation. The first two channels provide the boundary locations in the x and

y directions where pixel values $v \in [0, 1]$ are floating point to represent the distance to the nearest pixel in the x or y directions, respectively. For example, given the bottom left (x_{bl}, y_{bl}) and top right (x_{tr}, y_{tr}) floating-number coordinates of a rectangular patch, we compute the pixel indices as the floor,

$$\bar{x}_{bl} = \lfloor x_{bl} \rfloor, \bar{y}_{bl} = \lfloor y_{bl} \rfloor, \bar{x}_{tr} = \lfloor x_{tr} \rfloor, \bar{y}_{tr} = \lfloor y_{tr} \rfloor.$$

Then, we compute the values

$$v_l = 1 - (x_{bl} - \bar{x}_{bl}), v_r = x_{tr} - \bar{x}_{tr} \\ v_b = 1 - (y_{bl} - \bar{y}_{bl}), v_t = y_{tr} - \bar{y}_{tr}$$

where v_l, v_r, v_b, v_t correspond to the left, right, bottom and top boundary values, respectively. The left/bottom boundary is subtracted from 1 where as the right/top is not because the floor function has a subtly different semantic meaning between these cases; Without the loss of generality, the floor of the left/bottom boundary *is not* contained inside the interior of the patch whereas the floor of the right/top *is*. We chose this design as it enables sensible image dimensions (i.e. 60×300 for a $6\text{mm} \times 30\text{mm}$ image with a resolution of 10 pixels to 1mm) however others are possible. Finally, note, separating the x and y boundaries into two channels enables explicit representation of the corners of patches.

Finally, a third channel provides the *interior* of the antenna as a binary image where $v = 1$ for all index pairs x, y such that $x \in [\bar{x}_{bl} + 1, \bar{x}_{tr} - 1]$, $y \in [\bar{y}_{bl} + 1, \bar{y}_{tr} - 1]$ and $v = 1$. Please see Algorithm 1 for pseudocode of the process and Figure 2 for an example image. Some details are omitted such as patch dimensions which go beyond the board or overlapping patches but these are straightforwardly handled via clipping and masking.

Algorithm 1 ADD_PATCH_TO_IMAGE($x_{bl}, y_{bl}, x_{tr}, y_{tr}, image$)

Input: $x_{bl}, y_{bl}, x_{tr}, y_{tr}$: floating point bottom-left and top-right coordinates of rectangular patch, $image$: Image array

- 1: // Lower bound on coordinates to index image
 - 2: $\bar{x}_{bl} = \lfloor x_{bl} \rfloor, \bar{y}_{bl} = \lfloor y_{bl} \rfloor, \bar{x}_{tr} = \lfloor x_{tr} \rfloor, \bar{y}_{tr} = \lfloor y_{tr} \rfloor$
 - 3: // Write X boundaries
 - 4: $image_{x_bound}[\bar{y}_{bl} : \bar{y}_{tr}][\bar{x}_{bl}] = 1 - (x_{bl} - \bar{x}_{bl})$
 - 5: $image_{x_bound}[\bar{y}_{bl} : \bar{y}_{tr}][\bar{x}_{tr}] = x_{tr} - \bar{x}_{tr}$
 - 6: // Write Y boundaries
 - 7: $image_{y_bound}[\bar{y}_{bl}][\bar{x}_{bl} : \bar{x}_{tr}] = 1 - (y_{bl} - \bar{y}_{bl})$
 - 8: $image_{y_bound}[\bar{y}_{tr}][\bar{x}_{tr} : \bar{x}_{tr}] = y_{tr} - \bar{y}_{tr}$
 - 9: // Write interior
 - 10: $image_{interior}[\bar{y}_{bl} + 1 : \bar{y}_{tr} - 1][\bar{x}_{tr} + 1 : \bar{x}_{tr} - 1] = 1.0$
-

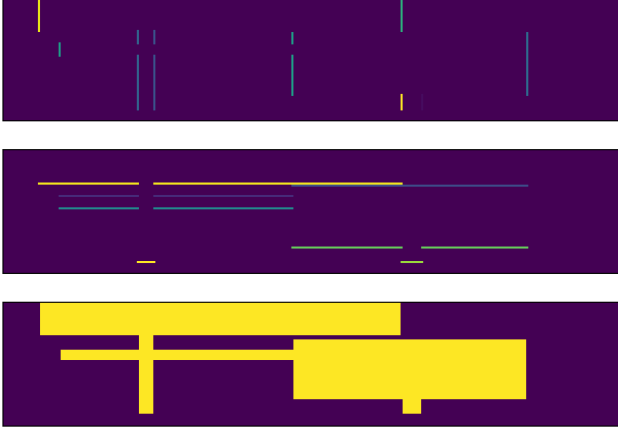


Figure 2. Three channel image representation. **Top:** Boundary values represent distance to nearest pixel in the x -direction. **Middle:** Boundary values represent distance to nearest pixel in the y -direction. **Bottom:** Binary interior of the antenna. This channel does not contain boundaries.

4.2. Surrogate Model

In this section, we propose an architecture for a surrogate model which predicts the zeros and poles directly from the image representation which is then used to compute scattering coefficients. The architecture is based on the Visual Transformer (Wu et al., 2020) which is motivated by the insight that local, spatial components such as boundaries between substrate of the antenna should be tokenized and then used by a transformer (Vaswani et al., 2017) to compute the global characteristics.

Given the input image $\mathbf{I} = \mathbf{I}(\mathbf{h}) \in \mathbb{R}^{3 \times HW}$ as a function of design choice \mathbf{h} , we first augment it with two additional channels of linearly spaced x and y coordinates (Liu et al., 2018), to yield augmented image $\hat{\mathbf{I}} \in \mathbb{R}^{5 \times HW}$. This is because the specific location of antenna components, in addition to its topology, determines the corresponding frequency response. Then, a CNN takes $\hat{\mathbf{I}}$ as an input and generates feature maps $\mathbf{X} \in \mathbb{R}^{HW \times C}$ where H , W and C are the height, width and channel dimension, respectively. A filter-based tokenizer (Zhang et al., 2019) generates L visual tokens $\mathbf{T} \in \mathbb{R}^{L \times C}$ by mapping each pixel via a point-wise convolution to L groups with matrix $\mathbf{W} \in \mathbb{R}^{C \times L}$ and computes a softmax in the pixel dimension

$$\mathbf{A} = \text{Softmax}_{HW}(\mathbf{X}\mathbf{W})$$

where $\mathbf{A} \in \mathbb{R}^{HW \times L}$ is referred to as an attention map. Visual tokens \mathbf{T} are computed via $\mathbf{T} = \mathbf{A}^T \mathbf{X}$ which is the weighted average of pixels in the original feature map \mathbf{X} . Intuitively, the tokens \mathbf{T} capture semantics such as relative boundary and corner locations and from this the transformer computes the global characteristic of the antenna configuration. Please see Figure 9 in Appendix D for a subset of

the learned attention maps for a specific antenna instance which demonstrate this.

After that, \mathbf{T} is then passed through a multi-layer transformer encoder (Vaswani et al., 2017), flattened and passed through a fully connected layer and a non-linearity. From this representation, three separate complex-valued fully connected layers predict the constant, zeros and poles. Concretely, let C_θ , Z_θ , P_θ be linear layers parameterized by θ . Then,

$$\begin{aligned} \mathbf{v} &= \text{FC}(\text{Transformer}(\mathbf{T})) \\ c_0(\mathbf{h}) &:= C_\theta(\mathbf{v}), \mathbf{z}(\mathbf{h}) := Z_\theta(\mathbf{v}), \mathbf{p}(\mathbf{h}) := P_\theta(\mathbf{v}) \end{aligned}$$

where \mathbf{h} is the design choice and $c_0(\mathbf{h})$, $\mathbf{z}(\mathbf{h})$, $\mathbf{p}(\mathbf{h})$ are the constant and vectors (of length K) of zeros and poles, respectively, used to compute the frequency response as per Equation 4. We refer to this architecture which outputs the constant, zeros and poles as **CZP**.

4.3. Model training

When training **CZP** models, we do not have direct supervision to $c_0(\mathbf{h})$, zeros $\mathbf{z}(\mathbf{h})$, and poles $\mathbf{p}(\mathbf{h})$, but only the $S_{11}(\omega)$ provided with CST Microwave Studio (CST, 2021) as ground truth. Therefore, we leverage Eqn. 4 to compute estimated $S_{11}(\omega)$ with c_0 , \mathbf{z} , and \mathbf{p} , so that it can match the ground truth. We then train the model via back-propagation in an end-to-end manner to minimize the Mean Squared Error (MSE), for frequencies in the range $[0.2 - 7.0]$ GHz at increments of 0.1 (i.e., 69 dimensions). We use a shrinkage loss (Li et al., 2018) variant of MSE as we found that with vanilla MSE, the model had higher error on the crucial parts of the scattering coefficients (i.e., the resonances).

5. Experiments

In this section, we demonstrate the impact of our architectural choices and image representation on the five patch example antenna discussed in Section 2.1. Specifically, we show that:

- Our proposed image representation is a significant improvement over reasonable coordinate-based inputs as well as a naive binary image input.
- The **CZP** formulation outperforms raw prediction when using the same transformer architecture proposed in Section 4 and the proposed image representation.
- The transformer architecture outperforms a CNN for the image representation and an MLP for coordinate based input.
- **CZP** generalizes well to unseen antenna designs, not only on a held-out dataset, but also as a surrogate model

for designs proposed by the reinforcement learning (RL) based search procedure, as verified to meet specific resonance requirements by commercial softwares.

5.1. Surrogate Modeling

We use 48K total samples, uniformly sampled and simulated with CST Microwave Studio (CST, 2021) where each sample takes between 90 and 120 seconds to simulate. 90% of samples are used for training and 10% are used for testing. From the training set, 10% are randomly sampled and used for validation. Each experiment is run for 3 random seeds. Appendix C provides all experimental hyperparameters.

Figure 3 illustrates the first set of experiments in which we demonstrate the effectiveness of (1) our novel image representation and (2) the proposed **CZP** when using the transformer architecture. To show (1), we compare against a coordinate-based method which concatenates the normalized bottom-left x, y coordinate of each patch with a one-hot vector to distinguish between patches. When using the transformer architecture, this generates 5 tokens, each with dimension 7. Before being processed by the transformer, each token is projected into a 256 dimensional vector by a 2-layer MLP with hidden layer of width 256. Additionally, to demonstrate (2), for both coordinate and image input, we compare against directly predicting the raw 69 dimensional frequency response with a fully connected layer, referred to as Raw in figures. Additionally, we ablate over different degree K of **CZP** with values 8, 12, 16, 20 and the number of attention layers L with values 8, 6, 4, 2.

First, within each configuration, the image representation improves over its coordinate counterpart by a minimum of 9.6% with $L = 4$ and raw prediction and a maximum of 26.8% with $L = 2$ and $K = 12$. Second, for the image representation, **CZP** improves over raw prediction by a minimum of 9.2% with $L = 8$ and $K = 12$ and a maximum of 28.0% with $L = 2$ and $K = 12$. For the coordinate representation, **CZP** improves over raw prediction by a minimum of 4.6% with $L = 8$ and $K = 12$ and a maximum of 25.1% with $L = 2$ and $K = 8$. Finally, increasing the transformer depth from 2 to 8 layers improves raw prediction for image and coordinate representations by 29.5% and 35.9%, respectively. Increased depth improves the **CZP** an average of 15.4% and 20.9% for image and coordinate representations, respectively.

From these statistics, we can extract the following insights which support the **CZP** architecture and image representation as powerful inductive biases; (1) With fewer transformer layers, **CZP** yields greater improvement over raw prediction and (2) **CZP** and image representation benefit *the least* from increasing the complexity of the model and, at the opposite extreme, raw prediction and coordinate representation benefit the most. These two points show that

without these inductive biases, deeper models are required as shallower models are likely to fall into local minima.

In Figure 4, we provide results for 4 other baselines to show the impact of the transformer and image representation over reasonable alternatives e.g., a fully connected MLP with coordinate input, a CNN with our image input, the transformer with a naive single-channel binary image input, and the Fourier Neural Operator (FNO) (Li et al., 2020) developed to solve other PDEs such as Navier-Stokes with image input. In the last row we reproduce the results of the 8-layer transformer with image input from Figure 3. The 8 layer transformer is a 40%+ improvement on these baselines.

Finally, in Figure 5, we provide a data ablation with raw prediction and **CZP** $K = 20$. The trend of **CZP** outperforming raw prediction holds in this setting as well although the differences in test loss are small. However, in the next section, we show that our model greatly outperforms the baselines when used for optimization when trained with less data, more robust for unseen designs. For other qualitative results such as attention map visualizations, please see Appendix D.

5.2. Optimization

In this section, we demonstrate the utility of the proposed model by showing it can be used by an optimization procedure to find antenna configurations that have specific resonance characteristics. This is a significant test of the generalization and robustness of the model since (1) an antenna with the desired resonances is *not* contained in the training set and (2) an optimization procedure can very easily find adversarial configurations to exploit the weaknesses of the surrogate model (Yuan et al., 2017). We hypothesize that **CZP** will be far more robust than raw prediction to these kinds of samples because it is by design smooth (i.e., a ratio of two polynomials) whereas raw prediction has no built in bias encouraging this property. Please see Figure 8 in Appendix D for qualitative intuition regarding this. In this section, we provide results which demonstrate that our proposed model, when used by an optimization procedure, has a significantly higher success rate and is more robust to dataset size than the baseline.

We frame antenna design as a reinforcement learning (RL) (Sutton & Barto, 1998) problem where an agent is tasked with sequentially placing each of the 5 patches such that the frequency response of the final antenna meets the resonance characteristics. Recall from Section 2, this means that the corresponding S_{11} is below a certain threshold at specific frequency ranges. In this problem, the frequency ranges are 2.4 GHz-2.5 GHz and 5.1 GHz-7.0GHz and the target thresholds are $t_{[2.4-2.5]} = -6.0$ dB and $t_{[5.1-7.0]} = -6.0$ dB, the spectrum for WiFi 6E.

Modeling Scattering Coefficients using Self-Attentive Complex Polynomials with Image-based Representation

Layers	Input Type	Raw	CZP $K=8$	CZP $K=12$	CZP $K=16$	CZP $K=20$
$L=8$	Image	.00284 \pm 7e-5	.00243 \pm 1e-4	.00258 \pm 3e-5	.00253 \pm 5e-5	.00234 \pm 2e-5
	Coord	.00327 \pm 5e-5	.003 \pm 8e-5	.00312 \pm 4e-5	.00307 \pm 4e-5	.00303 \pm 5e-5
$L=6$	Image	.00312 \pm 9e-5	.00254 \pm 3e-5	.00253 \pm 9e-5	.00255 \pm 6e-5	.00249 \pm 8e-5
	Coord	.00357 \pm 8e-5	.00308 \pm 9e-5	.00309 \pm 7e-5	.00313 \pm 8e-5	.00303 \pm 7e-5
$L=4$	Image	.00348 \pm 1e-4	.00268 \pm 7e-5	.00266 \pm 2e-4	.00251 \pm 5e-5	.00252 \pm 1e-4
	Coord	.00385 \pm 5e-5	.00317 \pm 6e-5	.00328 \pm 8e-5	.0032 \pm 1e-4	.00322 \pm 2e-5
$L=2$	Image	.00403 \pm 4e-5	.00292 \pm 1e-4	.0029 \pm 1e-4	.00294 \pm 1e-4	.00292 \pm 2e-4
	Coord	.0051 \pm 8e-5	.00382 \pm 2e-4	.00396 \pm 1e-4	.00385 \pm 5e-5	.00384 \pm 9e-5

Figure 3. Mean and standard deviation of the test loss over 3 seeds with the transformer architecture for *image* and *coordinate* input representations and $L=8, 6, 4, 2$ attention layers. Results are reported for raw frequency prediction and the **CZP** architecture with degree $K=8, 12, 16, 20$. In all configurations, the image representation outperforms coordinates and **CZP** outperforms raw prediction.

Arch + Input	Raw	CZP $K=8$	CZP $K=12$	CZP $K=16$	CZP $K=20$
MLP + Coord	.00492 \pm 5e-5	.00502 \pm 1e-4	.00553 \pm 3e-4	0.00507 \pm 3e-4	failed
CNN + Image	.0054 \pm 3e-5	.00496 \pm 1e-3	.00405 \pm 1e-4	.00424 \pm 1e-4	failed
Transformer + Binary Image	.0049 \pm 1e-4	.005 \pm 2e-4	.00488 \pm 9e-5	.00501 \pm 1e-4	.0049 \pm 8e-5
FNO + Image	.00724 \pm 5e-5	.00715 \pm 1e-4	.00706 \pm 5e-5	0.0073 \pm 2-4	.00724 \pm 9-5
Transformer + Image	.00284 \pm 7e-5	.00243 \pm 1e-4	.00258 \pm 3e-5	.00253 \pm 5e-5	.00234 \pm 2e-5

Figure 4. Mean and standard deviation of the test loss over 3 seeds for ablations of architectural components of the proposed model and baselines. Results reported are for raw prediction and **CZP** with degree $K=8, 12, 16, 20$ for the following configurations: 6-layer MLP with coordinate input, 5 layer CNN with image input, and 8 layer transformer with binary image input and 4-layer FNO with image input.

% Training Data	Transformer Out	
	Raw	CZP $K=20$
25%	.00621 \pm 3e-4	.00574 \pm 1e-4
50%	.00387 \pm 2e-4	.0038 \pm 2e-4
75%	.00329 \pm 1e-4	.00296 \pm 2e-4
100%	.00284 \pm 7e-5	.00234 \pm 2e-5

Figure 5. Mean and standard deviation of the test loss over 3 seeds for **CZP** $K=20$ and raw prediction with the 8-layer transformer architecture and image input with randomly sampled subsets of the training data for portions 25%, 50% and 75%. **CZP** has a lower test loss.

Formally, we define the state and action of the Markov Decision Process (MDP) (Puterman, 1994) as:

- **State:** A one-hot identifier and (x, y) coordinates of the bottom left corner of the patches which have been placed and a one-hot vector for the next patch to be placed.
- **Action:** (x, y) coordinates of the bottom-left corner of the next patch to be placed.

After all patches have been placed, the coordinates are converted to the image representation and the surrogate model predicts the frequency response $\log |S_{11}(\omega)|$. From the final

$\log |S_{11}(\omega)|$, we compute the following reward components for each resonance target.

$$r_{[2.4-2.5]} = \min(t_{[2.4-2.5]} - \log |S_{11}(\omega)|_{[2.4-2.5]}) \quad (5)$$

$$r_{[5.1-7.0]} = \min(t_{[5.1-7.0]} - \log |S_{11}(\omega)|_{[5.1-7.0]}) \quad (6)$$

where the subscripts correspond to list slicing. The sum $r = r_{[2.4-2.5]} + \min(1.0, r_{[5.1-7.0]})$ is then the reward given at the final timestep and at all previous timesteps the reward is zero. Note, we prevent the second reward component from being greater than 1.0 because in experiments the higher band (5.1 GHz-7.0 GHz) seemed to be easier to optimize and often led to local minima that did not optimize the lower band (2.4 GHz-2.5 GHz). To optimize, we use the implementation of Soft Actor Critic (SAC) (Haarnoja et al., 2018) from Stable-Baselines3 (Raffin et al., 2021) and build the environment using the Gym API (Brockman et al., 2016). Default hyperparameters are used except we perform two updates at the end of each episode as opposed to one or more updates per step.

For these experiments, we use the **CZP** $K=20$ and raw prediction architectures with an 8-layer transformer as these achieved the lowest test losses. For each of the 3 seeds for each architecture trained in the previous section, we run 3 seeds of RL optimization for a total of 9 experiments per configuration. In each experiment, we deploy the SAC agent

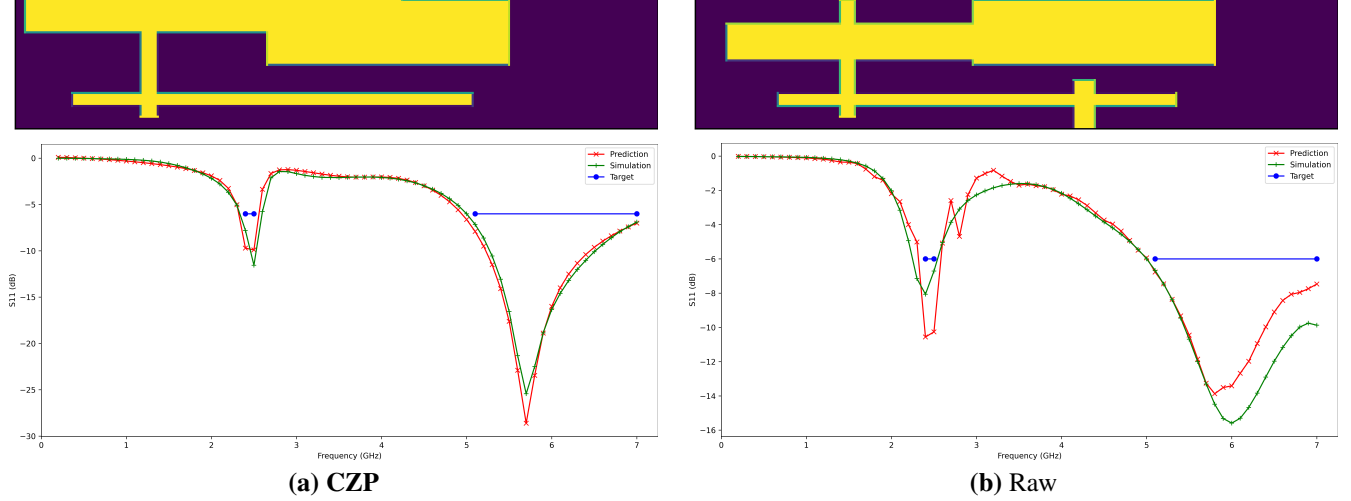


Figure 6. Two successful antenna configurations (top row) and corresponding frequency responses (bottom row) predicted by the model (red) and computed by CST (green) found by optimization via RL for (a) **CZP** and (b) **Raw**.

% Data	Transformer Out			
	Raw		CZP $K = 20$	
	% Top 3	Any Top 3	% Top 3	Any Top 3
25%	11.1%	22.2%	33.3%	55.6%
50%	14.8%	22.2%	40.7%	66.7%
75%	33.3%	55.6%	55.6%	77.8%
100%	51.9%	66.7%	88.9%	100%

Figure 7. Success rate for the % of top 3 configurations and if any of the top 3 configurations meet design requirements. Experiments performed for 3 seeds for RL for each of the 3 seeds of **CZP** $K = 20$ and raw prediction with the 8-layer transformer architecture and image input from the previous section. Experiments conducted also with randomly sampled subsets of the training data for portions 25%, 50% and 75%. **CZP** is more robust than raw prediction to the optimization procedure and to dataset size.

for 25K total episodes or 125K total timesteps (since the agent places 1 of 5 patches each step). We also investigate the robustness of this process to dataset size which is critical in the domain of antenna design as sample collection is expensive.

Generally, SAC is able to find antenna configurations which meet the requirements when using **CZP** and raw prediction architectures and in Figure 6 we provide examples in columns (a) and (b), respectively. The top row provides the found antenna configuration and the bottom row the frequency responses predicted by the model (red) and the CST simulation (green).

However, in terms of *success rate* (i.e., how many configurations or optimization runs actually produce an antenna which meets the constraints), **CZP** significantly outper-

forms raw prediction. Specifically, in Figure 7, we provide the percentage of the top 3 configurations (i.e., 3 per seed for a total of 27) found over all seeds which meet the constraints and also the percentage of runs where *any* of the top 3 meet the constraints. Additionally, we perform a data ablation to show that **CZP** is more robust to less data demonstrating its strength as an inductive bias.

6. Conclusion

In this work, we presented a novel surrogate model architecture to be used by optimization techniques for the problem antenna design. We first derived a theoretical form for the S_{11} scatter coefficients based on which we proposed the **CZP** network architecture. Additionally, as input to the proposed surrogate model, we proposed a novel image representation inspired by existing mesh-based simulation techniques. We then demonstrated experimentally that the proposed model and image representation are significant advances through architecture and data ablation studies. Finally, we showed that the proposed surrogate model had significantly higher utility in terms of success rate for optimization of antenna design than baselines.

Although the results are significant, the problem investigated in this work is still relatively simple compared to production level antenna systems. Future work will involve solving more complicated 2D problems as well as generalizing the proposed model and image representation to 3D antenna. Additionally, in this line of work, we plan to explore other tokenization schemes that are as information rich as images but are more computationally efficient since images require convolutions to featurize. Lastly, future work will involve the application to linear PDEs in general.

References

- Remcom. URL <https://www.remcom.com/xfdtd-3d-em-simulation-software/>.
- CST Studio Suite, 2021. URL <https://www.3ds.com/products-services/simulia/products/>.
- Bakr, M. H., Bandler, J. W., Madsen, K., and Rayas-Sanchez, J. E. Space-mapping optimization of microwave circuits exploiting surrogate models. *IEEE Transactions on Microwave Theory and Techniques*, 48:2297–2306, 2000.
- Brockman, G., Cheung, V., Pettersson, L., Schneider, J., Schulman, J., Tang, J., and Zaremba, W. Openai gym. 2016.
- Brown, T. B., Mann, B., Ryder, N., Subbiah, M., Kaplan, J., Dhariwal, P., Neelakantan, A., Shyam, P., Sastry, G., and Askell, A. e. a. Language models are few shot learners. In *Advances in Neural Information Processing Systems*, 2020.
- Caspers, F. Rf engineering basic concepts: S-parameters. *arXiv preprint arXiv:1201.2346*, 2012.
- Chilingaryan, G., Tamoyan, H., Tevosyan, A., Babayam, N., Khondaryan, L., Hambardzumyan, K., Navoyan, Z., Khachatrian, H., and Aghajanyan, A. Generative masked language models for molecular representations. In *arXiv preprint arXiv:2211.16349*, 2022.
- Dou, W., Tian, Y., Ye, G., and Zhu, J. Antenna artificial intelligence: The relentless pursuit of intelligent antenna design [industry activities]. *IEEE Antennas and Propagation Magazine*, 64, 2022.
- Haarnoja, T., Zhou, A., Abbeel, P., and Levine, S. Soft actor-critic: Off-policy maximum entropy deep reinforcement learning with a stochastic actor. In *Proceedings of the 35th International Conference on Machine Learning*, 2018.
- Koziel, S. Low-cost data-driven surrogate modeling of antenna structures by constrained sampling. *IEEE Antennas and Wireless Propagation Letters*, 16:461–464, 2017.
- Koziel, S. and Ogurtsov, S. Multi-objective design of antennas using variable-fidelity simulations and surrogate models. *IEEE Transaction on Antennas and Propagation*, 2013.
- Li, X., Ma, C., Ni, B., Yang, X., Reid, I., and Yang, M.-H. Deep regression tracking with shrinkage loss. In *European Conference on Computer Vision*, pp. 369–386, 2018.
- Li, Z., Kovachki, N., Azizzadenesheli, K., Liu, B., Bhattacharya, K., Stuart, A., and Anandkumar, A. Fourier neural operator for parametric partial differential equations, 2020.
- Liu, R., Lehman, J., Molino, P., Petroski Such, F., Frankl, E., Sergeev, A., and Yosinski, J. An intriguing failing of convolutional neural networks and the coordconv solution. In *Advances in Neural Information Processing Systems*, 2018.
- Pardo, D., Demkowicz, L., and Torres-Verdin, C. Paszynski, M. A self-adaptive goal-oriented hp-finite element method with electromagnetic applications. part ii: Electrodynamics. In *Computer methods in applied mechanics and engineering*, pp. 3585–3597, 2007.
- Pfaff, T., Fortunato, M., Sanchez-Gonzalez, A., and Battaglia, P. W. Learning mesh-based simulation with graph networks. In *International Conference on Learning Representations*, 2021.
- Puterman, M. *Markov decision processes: Discrete stochastic dynamic programming*. John Wiley & Sons Inc. New York NY USA, 1994. ISBN 0471619779.
- Raffin, A., Hill, A., Gleave, A., Kanervisto, A., Ernestus, M., and Dormann, N. Stable-baselines3: Reliable reinforcement learning implementations. *Journal of Machine Learning Research*, 22(268):1–8, 2021. URL <http://jmlr.org/papers/v22/20-1364.html>.
- Ramesh, A., Pavlov, M., Goh, G., Gray, S., Voss, C., Radford, A., Chen, M., and Sutskever, I. Generative masked language models for molecular representations. In *arXiv preprint arXiv:2102.12092*, 2021.
- Rayas-Sanchez, J. E. Em-based optimization of microwave circuits using artificial neural networks: the state-of-the-art. *IEEE Transactions on Microwave Theory and Techniques*, 52:420–435, 2004.
- Sutton, R. S. and Barto, A. G. *Reinforcement Learning: An Introduction*. The MIT Press, 1998.
- Vaswani, A., Shazeer, N., Parmar, N., Uszkoreit, J., Jones, L., Gomez, A. N., Kaiser, Ł., and Polosukhin, I. Attention is all you need. In *Advances in Neural Information Processing Systems*, pp. 5999–6009, 2017.
- Weiland, T. A discretization method for the solution of maxwell’s equations for six-component fields. In *Electronics and Communications AEU*, pp. 116–120, 1977.
- Wu, B., Xu, C., Dai, X., Wan, A., Zhang, P., Yan, Z., and Tomizuka, M. Visual transformers: Token-based image representation and processing for computer vision. In *arXiv preprint arXiv:2006.03677*, 2020.

- Yee, K. Numerical solution of initial boundary value problems involving maxwell's equations in isotropic media. *IEEE Transactions on Antennas and Propagation*, 14: 302–307, 1966.
- Yuan, X., He, P., Zhu, Q., and Li, X. Adversarial examples: Attacks and defenses for deep learning. In *arXiv preprint arXiv:1712.07107*, 2017.
- Zhang, S., He, X., and Yan, S. Latent-gnn: Learning efficient non-local relations for visual recognition. In *International Conference on Machine Learning*, pp. 7374–7383, 2019.
- Zhu, J., Bandler, J. W., Nikolova, N. K., and Koziel, S. Antenna optimization through space mapping. *IEEE Transaction on Antennas and Propagation*, 2007.

A. Derivations

Theorem 3.1 (Analytical Structure of Scattering Coefficients). *For ODE in the form of Eqn. 3, if $A(\mathbf{h})$ is diagonalizable, then the logarithm of modulus of the scattering coefficients $\log |S_{11}(\omega)|$ can be written as:*

$$\log |S_{11}(\omega)| = \log |c_0(\mathbf{h})| + \sum_{k=1}^K \log \left| \frac{\omega - z_k(\mathbf{h})}{\omega - p_k(\mathbf{h})} \right| \quad (4)$$

where the constant $c_0(\mathbf{h})$, zeros $\{z_k(\mathbf{h})\}_{k=1}^K$ and poles $\{p_k(\mathbf{h})\}_{k=1}^K$ are complex numbers and all depend on $A(\mathbf{h})$ and thus functions of the design choice \mathbf{h} .

Proof. Consider the following high-dimensional linear ODE problem of N variables:

$$\dot{\phi} = A\phi \quad (7)$$

Here ϕ is a N -dimensional vector and we refer its component at spatial location \mathbf{x} as $\phi(\mathbf{x})$ (i.e. a scalar), and A is an N -by- N diagonalizable matrix. $A = A(\mathbf{h})$ depends on material and topological properties, i.e., the design choice \mathbf{h} , is time-invariant and is not necessarily symmetric. Therefore, A has the following decomposition $A = U\Lambda U^{-1}$, where each column of U is its eigenvector and $\Lambda = \text{diag}(\lambda_1, \dots, \lambda_N)$ is a diagonal matrix containing all its eigenvalues $\{\lambda_i\}_{i=1}^N$. Note that entries of both U and Λ can be complex numbers. Since the ODE is stable and all excitation eventually vanishes, the real part of all eigenvalues are negative: $\Re[\lambda_i] < 0$.

By theory of linear ODE, we know that the solution to Eqn. 7 has analytic form:

$$\phi(t) = e^{At} \phi(0) \quad (8)$$

where $\phi(0)$ is the initial condition of ϕ . Then we can compute its (single-sided) Fourier transform $\hat{\phi}(\omega) := \int_0^{+\infty} \phi(t) e^{-i\omega t} dt$:

$$\begin{aligned} \hat{\phi}(\omega) &= \left(\int_0^{+\infty} e^{At} e^{-i\omega t} dt \right) \phi(0) \\ &= U \left(\int_0^{+\infty} e^{\Lambda t} e^{-i\omega t} dt \right) U^{-1} \phi(0) \\ &= U \text{diag} \left(\int_0^{+\infty} e^{\lambda_i t} e^{-i\omega t} dt \right) U^{-1} \phi(0) \\ &= U \text{diag} \left(\frac{1}{i\omega - \lambda_i} \right) U^{-1} \phi(0) \end{aligned} \quad (9)$$

Note that U and $\phi(0)$ are all time-invariant.

For double-sided Fourier transform $\hat{\phi}(\omega) := \int_{-\infty}^{+\infty} \phi(t) e^{-i\omega t} dt$ and symmetric signal extension

$\phi(-t) = \phi(t) = e^{A|t|} \phi(0)$ to negative side, similar we can compute

$$\int_{-\infty}^{+\infty} e^{\lambda_i |t|} e^{-i\omega t} dt = \frac{1}{i\omega - \lambda_i} + \frac{1}{-i\omega - \lambda_i} \quad (10)$$

$$= -\frac{2\lambda_i}{\lambda_i^2 + \omega^2} \quad (11)$$

Note that while it looks like a real number, the result is still complex since the eigenvalue λ_i is in general a complex number for an asymmetric dynamical system A . In this case, we can write $\hat{\phi}(\omega)$ as:

$$\hat{\phi}(\omega) = -U \text{diag} \left[\frac{2\lambda_1}{\lambda_1^2 + \omega^2}, \dots, \frac{2\lambda_N}{\lambda_N^2 + \omega^2} \right] U^{-1} \phi(0)$$

In both cases, each component of $\hat{\phi}(\omega)$ is a rational function of complex polynomial with respect to frequency ω . Since all voltages and currents in the antenna are linear functions of EM quantities represented in the components of ϕ , they are also rational function of complex polynomials. As a result, the input impedance $Z_{\text{in}}(\omega)$ of the antenna, defined as the ratio between the voltage and the current, is also a rational function of complex polynomials, represented as a quotient of two complex polynomials $Q_1(\omega)$ and $Q_2(\omega)$:

$$Z_{\text{in}}(\omega) = \frac{Q_1(\omega)}{Q_2(\omega)} \quad (12)$$

Note that this holds regardless of where the voltage and the currents are defined.

Therefore, the scattering coefficient $S_{11}(\omega)$ has the following structure:

$$S_{11}(\omega) := \frac{Z_{\text{in}}(\omega)/Z_0 - 1}{Z_{\text{in}}(\omega)/Z_0 + 1} = \frac{Q_1(\omega) - Z_0 Q_2(\omega)}{Q_1(\omega) + Z_0 Q_2(\omega)} \quad (13)$$

Therefore, it can be represented as a ratio of two complex polynomials of the *same* degrees (called it K).

According to the fundamental theorem of algebra, any polynomial of order K can be written as a product of order-1 factors $\omega - \omega_k$ and a constant, where $\{\omega_k\}$ are the (complex) roots of the K -th order polynomials. Therefore, the log spectrum of $S_{11}(\omega)$ is:

$$\log |S_{11}(\omega)| = \log |c_0(\mathbf{h})| + \sum_{k=1}^K \log \left| \frac{\omega - z_k(\mathbf{h})}{\omega - p_k(\mathbf{h})} \right| \quad (14)$$

where the constant $c_0(\mathbf{h})$, zeros $\{z_k(\mathbf{h})\}_{k=1}^K$ and poles $\{p_k(\mathbf{h})\}_{k=1}^K$ are all functions of $A = A(\mathbf{h})$ and thus the design choice \mathbf{h} . \square

Remark. Note that it is possible that the polynomial $Q_1(\omega) - Z_0 Q_2(\omega)$ may not have the same order as the

polynomial $Q_1(\omega) + Z_0 Q_2(\omega)$ (i.e., one of them has their leading term precisely cancelled out, while the other does not). While this is a rare situation, when it happens, Eqn. 14 still applies, by having one or more zeros/poles moving far away from the concerned frequency region of ω . Then the corresponding factor $|\omega - z_k|$ (or $|\omega - p_k|$) almost never changes, and can be absorbed into the constant term c_0 .

B. Specification of the Design Space

The dimensions $s_k = (s_{k,x}, s_{k,y})$ and ranges for the location $l_{k,x}, l_{k,y}$ of each of the 5 patches p_k are

$$\begin{aligned} p_1: s_1 &= (0.75, 5.49), l_{1,x} \in [0, 10], l_{1,y} \in [0.5, 0.5] \\ p_2: s_2 &= (17.64, 1.7), l_{2,x} \in [0, 12.36], l_{2,y} \in [1, 4.7] \\ p_3: s_3 &= (11.38, 3.0), l_{3,x} \in [10, 18.62], l_{3,y} \in [1, 3] \\ p_4: s_4 &= (18.63, 0.56), l_{4,x} \in [0, 11.37], l_{4,y} \in [1, 5.44] \\ p_5: s_5 &= (0.99, 2.43), l_{5,x} \in [10, 29.01], l_{5,y} \in [-2, 3.57] \end{aligned}$$

where all values are in mm. These values were determined from antennas that have been used for past production devices in industry. Additionally, patch p_1 determines the location of the discrete port.

C. Experimental details

Hyperparameter	Value
Batch Size	100
Learning Rate	.0005
Activation	Swish
Warmup epochs	100
Decay LR plateau epochs	20
Decay LR plateau factor	.5
Total Epochs	500
Attention heads	8
Attention layers	[2,4,6,8]
CZP Degree	[8,12,16,20]

Table 1. General experimental hyperparameters

Hyperparameter	Value
Spatial Attention Maps	16
Conv KernelxStridexPad	5x1x2
Conv Layers	2
Conv Filters	128
Attn dim_feedforward	256

Table 2. Image input specific hyperparameters for the transformer with spatial attention

Hyperparameter	Value
FC embed dimension	256
FC layers	2
Attn dim_feedforward	512

Table 3. Coordinate input specific hyperparameters for the transformer with coordinate input

D. Other Visualizations

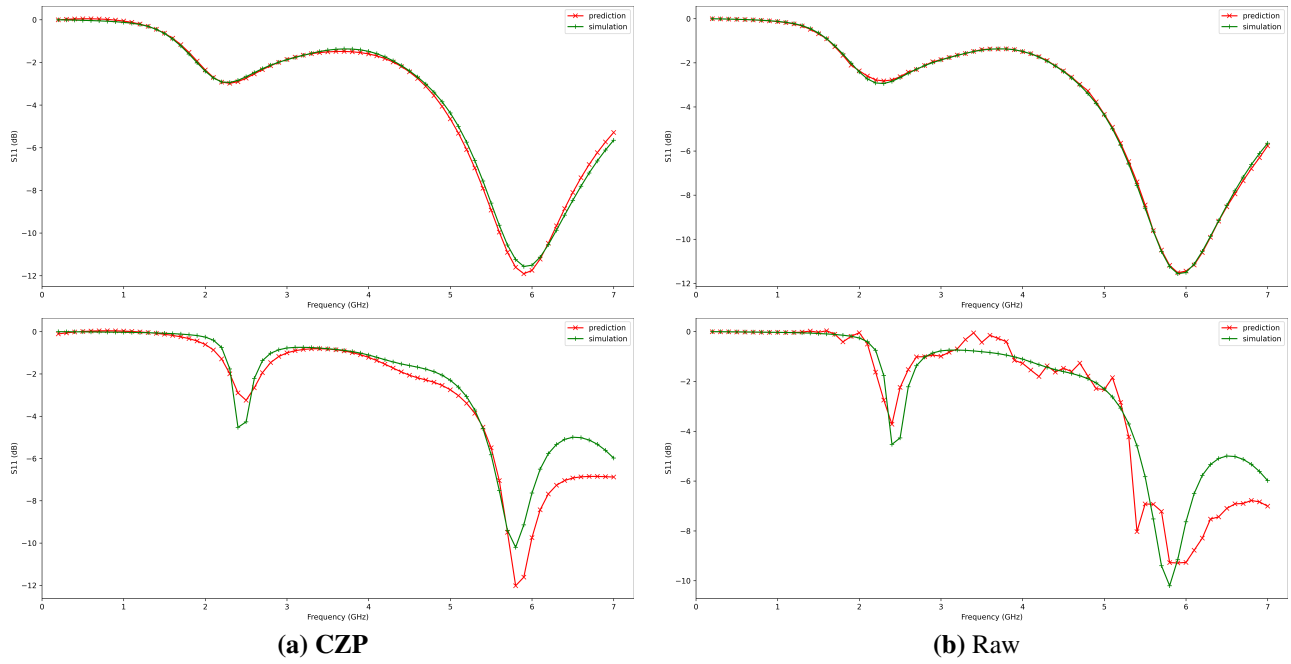


Figure 8. Comparison of predicted frequency response (a) CZP and (b) Raw with an 8 layer transformer and image input on two *test set* examples, with low MSE (top row) and high MSE (bottom row). Red is the frequency response predicted by the surrogate model, green is the frequency response from CST. For easy examples, CZP and raw are both smooth. For hard examples, CZP is smooth by design but raw may be non-smooth.



Figure 9. A random antenna configuration (above line) and four (of sixteen total) attention maps (below line) learned by the spatial attention component of the proposed transformer architecture (overlayed on the antenna configuration). The intensity of the red shading indicates the activations of the attention map. Activations are greatest around boundaries and corners.